Ee

CNS Report

Development of the Flattop Accelerated Beam

for Low-Energy Radioisotope Beam Separator CRIB

S. Watanabe, T. Teranishi, H. Iwasaki, Y. Yanagisawa, Y. Ohshiro, T. Katayama,

A. Goto, S. Kohara, N. Sakamoto, O. Kamigaito, M. Kase, Y. Yano, and M. Fukuda

Technical report on Accelerator and Instrumentation

Development of the Flattop Accelerated Beam
for Low-Energy Radioisotope Beam Separator CRIB

S. Watanabe[a*], T. Teranishi[a], H. Iwasaki[a], Y. Yanagisawa[b], Y. Ohshiro[a], T. Katayama[a],

A. Goto[b], S. Kohara[b], N. Sakamoto[b], O. Kamigaito[b], M. Kase[b], Y. Yano[b], and M. Fukuda[ac]

[a] *Center for Nuclear Study, Graduate School of Science, University of Tokyo, RIKEN campus,*

Hirosawa 2-1, Wako, Saitama, 351-0198 Japan

[b] *RIKEN(The Institute of Physical and Chemical Research), Hirosawa 2-1,*

Wako, Saitama, 351-0198 Japan

[c] *Takasaki Radiation Chemistry Research Establishment, JAERI,*

Watanuki 1233, Takasaki, Gunma, 370-1292 Japan

*e-mail: watasin@cns.s.u-tokyo.ac.jp

Abstract

This paper introduces the flattop acceleration system in the RIKEN-AVF cyclotron, which has been constructed at Center for Nuclear Study (CNS), University of Tokyo as a part of CNS-RIKEN collaboration. The system is almost ready for operation. The technique and hardware of the flattop acceleration for RIKEN-AVF cyclotron is described. An experimental result of development of the flattop-accelerated beam is also discussed.

1. Introduction

The RIKEN-AVF cyclotron provides a variety of heavy-ion beams with energies up to about 10 MeV/nucleon and intensities as high as 300 pnA. In 2001, a flattop acceleration system in the RIKEN-AVF cyclotron (K-70) was constructed and installed to improve the beam quality. There are two flattop resonators. The newly constructed flattop resonators are installed beside the existing main resonators. The third harmonics voltages generated by the flattop resonators are superimposed on the fundamental voltages so as to make the flattop regions in the accelerating voltages. It is turned out that an injected beam meet the flatten voltages during passes through the acceleration gaps in every passing time. A stable accelerating voltage as well as a good magnetic field promise the better quality beam for the nuclear physics experiments. So the installation of the flattop acceleration system is a key word of the improvement of beam quality in the RIKEN-AVF cyclotron. After the installation of the flattop acceleration system, quality of the flattop-accelerated beam was confirmed by using a magnetic beam analyzer such as a low-energy RI beam separator, called CRIB. The CRIB is an in-flight separator, installed in the RIKEN Accelerator Research Facility (RARF) [1]. The present paper discusses the flattop acceleration system installed in the RIKEN-AVF cyclotron as well as beam quality measured by the CRIB. The improvement of the magnetic field will be discussed elsewhere. Construction of the flattop acceleration system and development of the flattop-accelerated beam were completed as a part of the CNS-RIKEN collaboration.

2. RIEKN-AVF cyclotron

The RIKEN-AVF cyclotron is used for ions mainly from proton to light heavy ions like Argon. The rf system for ordinary acceleration of the RIEKN-AVF cyclotron has been working well after its completion in March 1989. A layout of the RIEKN-AVF cyclotron without the flattop acceleration system is shown in Fig. 1. The injection and the extraction radii are 1.64 cm and 71.4 cm, respectively. The initial phase of the beam is made less than $\pm 10^\circ$ with a phase defining slit. The RIEKN-AVF cyclotron has two resonators, each of which is the coaxial quarter-wave length type with a Dee angle of 83°. The fundamental frequency range (f_0) is from 12 to 24 MHz. The required maximum accelerating voltage of each resonator is 50 kV. A grounded-cathode tetrode (4CW50000E) amplifier is capacitively coupled to each resonator with a fixed coupling capacitor. Its maximum output power is 20 kW.

The flattop acceleration system in the RIEKN-AVF cyclotron has been designed so as to make the flattop region in the accelerating voltage. The design principle to make the flattop region is to impose either the third or fifth harmonic voltage on the ordinary accelerating voltage [2]. In order to impose the harmonic voltage on the Dee, the RIKEN accelerator development group has studied a cold model test in details. After the cold model test, the flattop acceleration system using the third harmonic resonator has been designed and constructed as a part of the CNS-RIKEN collaboration [3]. The specification of the flattop acceleration system is determined on the basis of the requirement to the beam quality such as the energy spread and the extraction efficiency. A flattop voltage, a structure and electrical characteristics of the flattop acceleration system are given in Chapter 3.
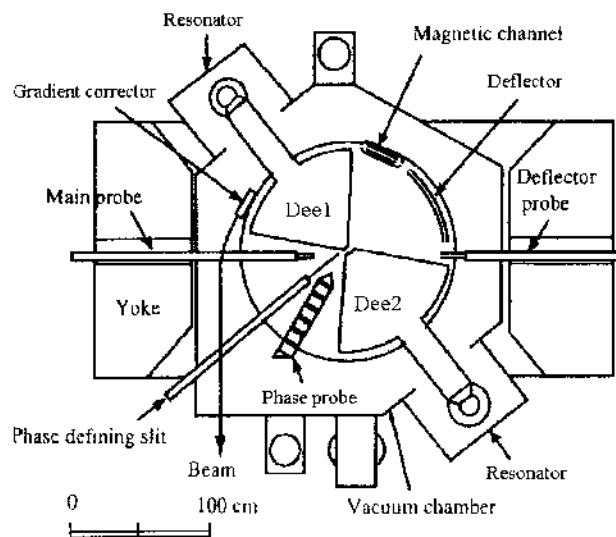

Fig. 1: Layout of the RIKEN-AVF cyclotron [2]. There are three kinds of the beam probes. The main probe seeks turn separation of the accelerated beam in the cyclotron. The phase probe detects the accelerated beam on the isochronous orbit along the moving radii. The deflector probe seeks the beam on the extraction orbit.

3. Flattop acceleration system

3-1 Flattop accelerating voltage

The flattop accelerating voltage is generated by a superposition of the fundamental and 3rd-harmonic frequencies.

The fundamental-frequency (f_0) range is from 12 to 24 MHz; the 3rd-harmonic frequency ($3f_0$) range is designed from 36 to 72 MHz. Before designing the real system, we measured the rf characteristics in detail using a model and found that the power loss for the 3rd harmonics was actually less than that for the 5th harmonics [4].

A flattop region near the top of accelerating voltage is designed as shown in Fig. 2 according to the formulae of

$$V_3 = V_1 \cos (2\pi f_0 t) - V_2 \cos (2\pi 3 f_0 t)), \qquad (1)$$

where the V_1 and V_2 are a peak voltage of the fundamental to be generated on a Dee gap, and 1/9 of the fundamental voltage, V_1, respectively.

The stability of flattop voltage, V_3, is to be set within 0.1% to attain the energy spread of the beam less than 0.2%. Two sets of the flattop acceleration system have been constructed because of the symmetrical two Dees system. The phase matching and voltage control of the flattop accelerating voltages are crucial to achieve the high-resolution beam. An electric discharge voltage due to the superimposition both of the rf voltages is to be investigated in this study.
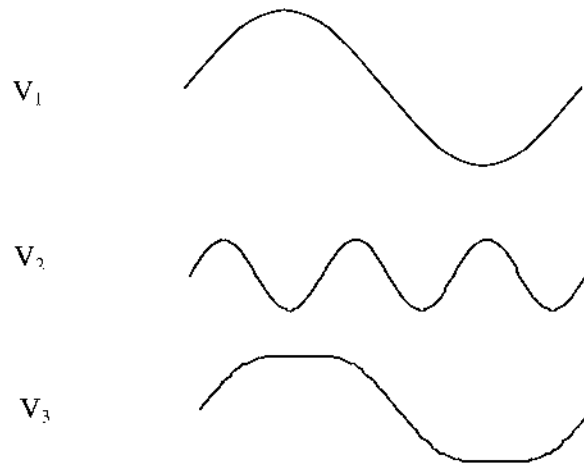

Fig. 2: Schematic drawing of the flattop accelerating voltage (V_3). The V_1 and V_2 are superimposed to make the V_3. The formula of superimposition is given in the paper.

3-2 Structure of flattop resonator

Cross-sectional views of the system are shown in Fig. 3. The flattop resonator shown inside the square of dashed line is designed to be a coaxial resonator with a movable shorting plate, and is coupled with the main resonator shown in the left hand side of Fig. 3 via the coupling capacitor (Cc). The coupling capacitor is made of copper plate with a size of 150 mm in width and 150 mm in height. It makes the combined systems that resonate at both fundamental and 3rd-harmonic frequencies simultaneously. The rf power of the 3rd harmonics is fed through a variable capacitor (Cf), which matches the input impedance of the flattop resonator to the impedance of the feeder. The amplitude and phase of the 3rd harmonics across the Dee gap are adjusted to produce a voltage proportional to the formula (1). The main resonator is the coaxial resonator with quarter-wave length type. The movable shorting plate as shown in Fig.3 realizes a reentrant structure. This shorting plate changes the resonance frequency from 12 to 24 MHz. The

capacitive tuner carries out a fine-tuning of the resonance frequency of the main resonator. The accelerating voltage on the Dee is appeared as maximum amplitude of the quarter-wave at the resonance frequency. The generated accelerating voltage is pick-upped by the Dee-voltage pickup. The pick-upped voltage is depend on the position of the Dee-voltage pickup since the amplitude of the quarter-wave is appeared as function of electric length from the reentrant position of the main resonator. The capacitive coupling, Cc, which is voltage feeder to the main resonator, is positioned where the amplitude of the quarter-wave is smaller than the Dee tips. The gap of Cc is adjusted so as to maximize the transmission power from the flattop cavity to the main resonator. The gap of Cc is set as small value as possible in the range that does not cause electric discharge. The physical dimensions of the flattop resonator are listed in Table 1. The listed parameters are determined on the basis of the cold model test and are referred in the design of the real model of the flattop resonator.
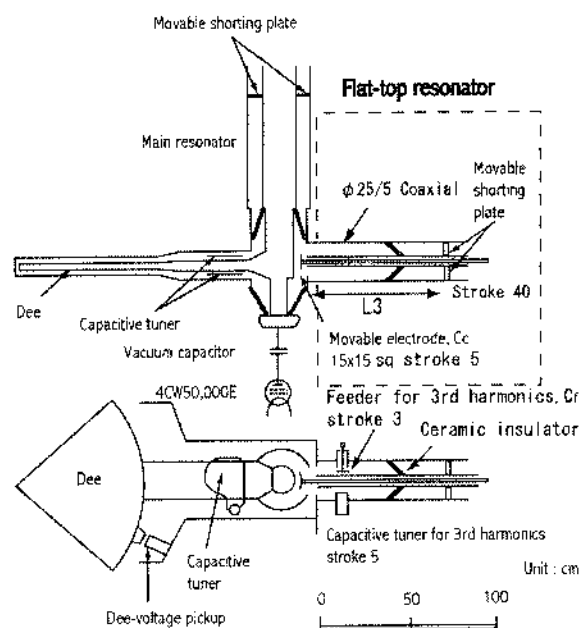

Fig. 3: Main resonator and flattop resonator. Upper and lower figures show vertical and horizontal section, respectively. Movable length of flattop resonator is shown as L3 [4].

Table 1. Physical dimensions of flattop resonator

Resonance frequency	36-72 MHz
Length of resonance resonator	1000 mm
Outer conductor ID	250 mm
Inner conductor OD	50 mm
Shorting plate stroke	400 mm
Coupling capacitor stroke	50 mm
Capacitive feeder stroke	30 mm
Capacitive tuner stroke	50 mm

3-3 Cold model test

In a cold model test, the resonance of 3rd-harmonic voltage was measured to see if the required frequency range could be achieved. In the measurement, both the coupling capacitor (Cc) and the movable shorting plate of flat-top resonator (L3) were adjusted after the movable shorting plate of main resonator (Lavf) was set for the fundamental frequency. In this case, the signal of 3rd-harmonic-frequency is fed into the flattop resonator through the voltage pick-up of 3rd-harmonic frequency and was monitored by the Dee-voltage pickup. It was found that the 3rd-harmonic resonant frequency was successfully generated on the Dee in the whole required frequency-range along with the fundamental-resonant frequency. The positions of the movable shorting plates of the flattop and main resonators were measured as a function of the 3rd-harmonic-resonant frequency.

Fig. 4 shows a resonance mode of the flattop acceleration system illustrated in Fig. 3. The $3/4\lambda$ mode resonances, f1 and f2, are plotted in the Fig. 4. The f1 and f2 intersect the lines f0x3 and f0x5, respectively. Parasitic resonance's (f4 and f5) are also plotted. We found that the 3rd resonance mode, f1, is a candidate of our flattop resonator. The measured Q-value (Q0) of the fundamental mode was found to vary from 1200 to 2400, while the measured Q-value of the 3rd-harmonic mode was from 720 to 1250. The Q-value of 5th-harmonic mode (f2) was lower than the 3rd-harmonic mode at the required resonance frequency.
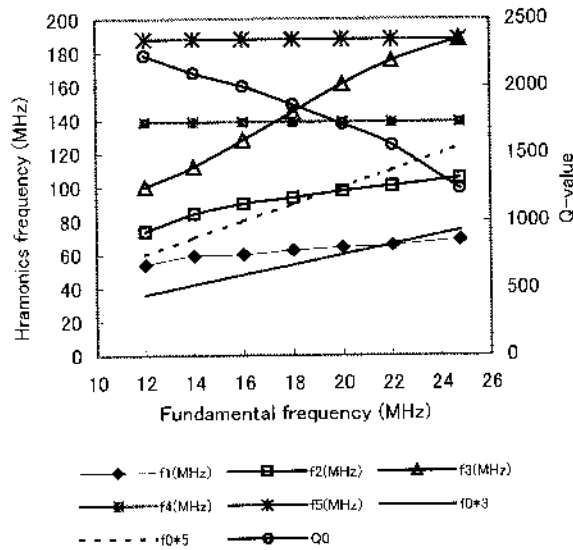

Fig. 4: Measured Q-values (Q0) of the fundamental frequency. The 3rd-harmonic mode (f1) intersects a line f0x3 as well as intersection of lines f0x5 and f2.

Frequency coverage of the capacitive tuner is expected as a wide enough to compensate a frequency shift due to heat in normal operation. In the cold model test, feeding low-level signals of the fundamental and 3rd-harmonic frequencies at the same time generates the flattop accelerating voltage. In this case, the fundamental-frequency signal was fed into the resonator through the vacuum capacitor, while the 3rd-harmonic-frequency signal was fed into the resonator through the capacitive feeder of flattop resonator. The theoretical 3rd-harmonic resonance voltage for superimposition is $V_0/3^2$ where V_0 the fundamental voltage. The flattop accelerating voltage generated on the Dee was

measured by the voltage pickup. The amplitude and phase of the 3rd-harmonic frequency signal were adjusted to obtain the flattop voltage on the Dee after those of the fundamental-frequency signal were fixed. It was found that the flattop voltage could be generated in the whole frequency range.

The measured resonance was found to be very close to the frequency 3 times as large as the fundamental frequency. This result gives the specifications of flattop resonator, which proves achievement of the required frequency range. We also discussed fine-tuning of the flattop voltage along Dee radii in order to flatten the extracted beam energy.

3-4 Commissioning of the flattop resonator

The real model of the flattop acceleration system was installed in the RIEKN-AVF cyclotron. There are two systems called No.1 and No.2 flattop systems, respectively. The photo of No.2 flattop resonator is shown in Fig.5. The flattop resonator installed beside the existing main resonator. The power amplifier, 4CW50000E, for main resonator is set in the electromagnetic shield box. Tuning for the fundamental frequency is performed in the main resonator and then that for the 3rd harmonics is carried out both with a shorting plate (L3) and the coupling capacitor (Cc). These tunings interfere with each other. The resonance of the 3rd harmonics is kept constant automatically with a capacitive tuner of the 3rd harmonics detecting the forward and reflected waves on the feeder line. The stroke of the capacitive tuner is 50 mm. Whole tuning devices are driven by the synchronous motors. In order to detect the tuning position, the rotated precision potentiometer has been used. A ceramics insulator is used for support of an inner conductor of a coaxial resonator also for achieving a vacuum seal. The flow rate of cooling water for each flattop resonator is 9 l/min.
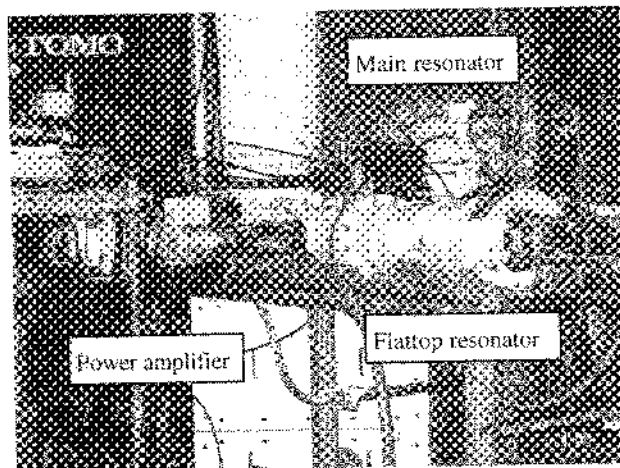

Fig. 5: Flattop resonator installed beside the existing main resonator. This photo shows the No.2 resonator. The power amplifier, 4CW50000E, for main resonator is set in the electromagnetic shield box.

Relationships between the tuning elements and the resonant frequencies have been measured by using a network analyzer. The optimum values for a combination of these two parameters were searched so that the transmission efficiency became the largest. It was found that the 3rd-harmonic resonance was limited below 63.3 MHz and did not reach the required highest frequency. For the frequencies higher than 63.3 MHz, we plan to retest with a reduction in the size of the coupling capacitor (Cc). A coupling coefficient of the newly designed voltage pick-up for the Dee voltage

detection was measured. The rf powers for the required maximum voltages of the 3rd harmonics were estimated.

The measured coupling coefficient of the voltage pick-up for the Dee voltage detection are different for the No. 1 and No. 2 resonators; the causes of this difference are under investigation. The measured frequency change covered by the capacitive tuner for the 3rd harmonics was about 1%. The frequency change of the fundamentals was negligible in this measurement.

3-5 High power test

The power test was carried out to generate specific flattop voltage on the Dee. Driving powers of the fundamental and the 3rd-harmonic frequencies were fed into the resonator simultaneously after setting the parameters of the flattop resonator to their own optimum positions [4]. An rf power amplifier for the flattop resonator is shown in Fig. 6. The low-level rf electronics and control system are set near the rf amplifiers. The measurement and adjustment of the low-level rf electronics system were carried out by a manual operation on the graphical control panel. A remote operation is available from the RRC control room.
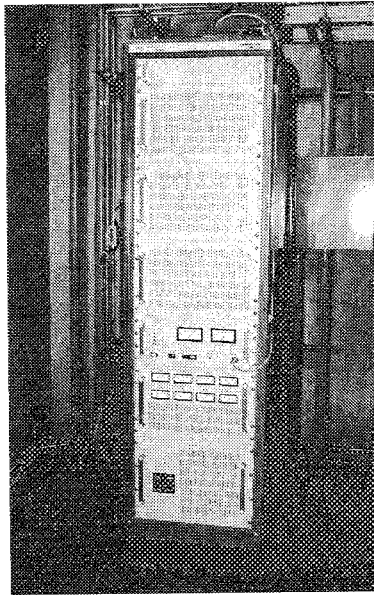

Fig. 6: The rf amplifier for No.1 flattop resonator. The maximum output power rating is 5 kW. The gain of rf amplifier is 57+/-2 dB and dynamic range is 20 dB, respectively. The rf amplifier for No.2 flattop resonator also has the same structure and specification.

A typical waveform of the flattop voltage of the No. 2 resonator is shown in Fig. 7. Total noise ratio, R, in the accelerating voltage is expressed by

$$R = \left(P_s + P_n\right)/P_c = \left(\int_{f1}^{f2} V_s^2(f)df + \int_{f1}^{f2} V_n^2(f)df\right)\Big/P_c , \qquad (2)$$

where P_s, P_n, P_c are power levels of a side-band wave, a ripple noise, and a carrier wave, respectively.

A signal-generator of the rf acceleration system requires the carrier wave with excellent purity level as well as precise frequency resolution. The tested signal generator (Anritsu MG440A) provides a carrier-side band level, P_s/P_c, of −80 dBc. The ripple noise is mainly comes from a power supply of the rf power amplifier. The side-band wave due to mechanical vibration of the Cryo-pump was found around the third harmonic frequency detected by the voltage-pickup of the third harmonic resonator. The detected side-band wave was $3f_0 \pm 200$ Hz. After exchange the Cryo-pump system into the low-vibration type, the side-band ripple in the detected Dee voltage is disappeared. The whole voltage stability less than 0.1 % has been attained in the accelerating voltage.

An electric discharge due to Multipactling phenomena is predictable around the high-voltage rf devices. Commissioning of the high power rf system is proceeded step by step, especially in the build up process of the rf accelerating voltage. Firstly, the pulsed rf voltage is applied to accelerating gap. After the confirmation of stable rising of the accelerating gap voltage, constant rf voltage is applied to the accelerating gap. Fig. 7 shows flattop voltage that the fundamental frequency is 16.3 MHz and the 3rd-harmonic frequency is 48.9 MHz. The fundamental voltage was 50 kV.
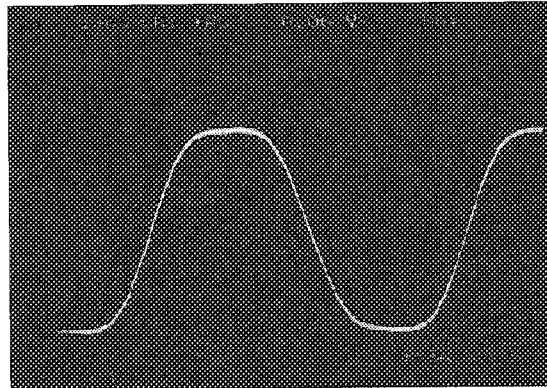

Fig. 7: Typical waveform of the flattop voltage measured by the Dee-voltage pickup.
The fundamental frequency was 16.3 MHz and the 3rd-harmonic frequency was 48.9
MHz. The fundamental voltage was 50 kV.

A small view-port is prepared beside the sidewall of the cyclotron vacuum chamber. We measured the X-ray flux level in direction of the view-port axis. When the flattop excitation power of 4.3 kW at 48.9 MHz is fed into the flattop cavity, GM counter detects the X-ray level up to 1000 Kcps at 30 cm apart from the surface of view-port. The small view-port is then covered with Pb plate with 1 mm thickness as the radiation shield.

A forwards and reflected rf power at the output port of the rf power amplifier of the flattop acceleration system are detected. If the detected phase difference between the forwards and reflected rf power is negative compared with standard phase difference, the capacitive tuner for 3rd harmonics resonator is controlled so that the phase difference becomes the minimum value. The volume deformation of the rf cavity is expected because of rf power dissipation. The capacitive tuner plays a roll to minimize an rf loss in the wakeup process and long-term compensation process.

4. Development of flattop accelerated beam

4-1 Beam acceleration

We have undertaken beam development to improve the energy spread of the beam. We have investigated the beam properties of the flattop acceleration using a 6.4 MeV/u $^{14}N^{6+}$ beam. The energy distribution of the accelerated particles was directly observed by using the magnetic beam analyzer, called CRIB, installed in E7 course [5]. We made a comparison of the energy spread of the beam between the flattop acceleration and ordinary acceleration using a sinusoidal voltage waveform.

In the RIKEN-AVF cyclotron, a peak Dee voltage of the ordinary acceleration is determined by a constant orbit method [6]. The central region of the cyclotron was designed to accelerate the particles passing through the first acceleration gap between an inflector and a puller at the RF phase of −30 degrees before reaching to the peak voltage. A particle trajectory in the central region is shown in Fig. 8.
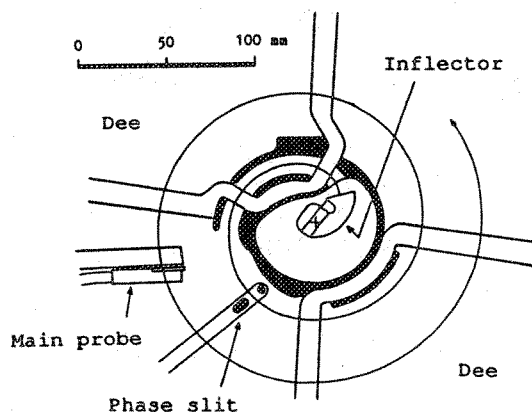

Fig. 8: Particle trajectory in the central region of the RIKEN-AVF cyclotron [6]. The accelerating voltage at first acceleration gap, which countered the exit of inflector, gives the first energy gain to the injected beam that came out of inflector. The phase slit defines the beam sizes of the injected beam.

In order to keep the trajectory constant and to avoid the beam loss in the central region, the energy gain at the first acceleration gap for the flattop acceleration is required to correspond to that for the ordinary acceleration. The voltage waveform for the flattop acceleration using the third harmonics is shown in Fig. 9. The flattop voltage is given by

$$V(\theta) = V_{peak}\left(\cos\theta - \frac{1}{9}\cos(3\theta)\right), \tag{3}$$

where V_{peak} is the peak value of the fundamental voltage, θ the RF phase.

The voltage at the phase of −30 degrees RF is invariable even if the third-harmonic waveform is superimposed on the fundamental one. Thus the energy gain at the first acceleration gap is the same as the ordinary accelerating voltage.

In this study, the fundamental voltage of 36.5 kV at a frequency of 15.6 MHz was applied for the 6.4 MeV/u $^{14}N^{6+}$ beam. The optimum third-harmonic voltage for the flattop acceleration was 4.1 kV. Thus V_{Dee} at flattop voltage is calculated at 36.5-4.1=32.4 KV. An expected overall turn number of the flattop acceleration increases by 11 %, since it is inversely proportional to the peak voltage. The detail of turn separation is given Chapter 7.

The bunch structure of the beam extracted from the cyclotron was investigated with the beam phase monitor using a micro channel plate (MCP) installed in the beam transport line. Single turn extraction was clearly observed by the MCP in conjunction with beam sawing system in the injection line.
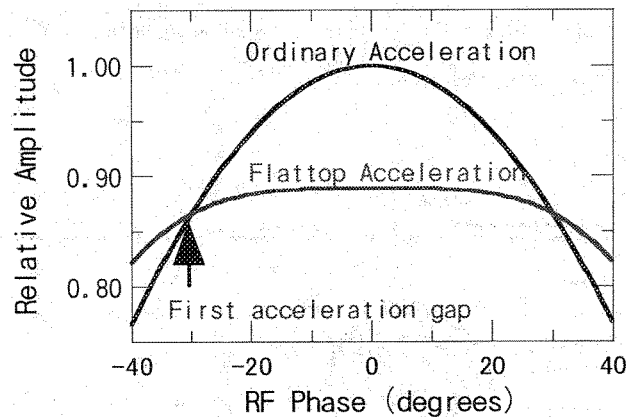

Fig. 9: Voltage waveforms of the ordinary acceleration and the flattop acceleration using the third harmonics. The injected beam receives accelerating energy at the first acceleration gap.

4-2 Magnetic beam analyzer CRIB

The CRIB and their beam transport line were constructed as a part of CNS-RIKEN collaboration [5][7]. The configuration of the CRIB is shown in Fig. 10. The CRIB consists of seven magnets and two focal planes with a configuration of F0-Q1-M1-D1-Q2-F1-D2- M2-Q3-F2, where F0 is the production target position as the in-flight RI beam separator. It is designed that the dispersive focused RI beam at F1 is to be focused at F2 whenever the achromaticity is established completely. Short-lived nuclei produced by nuclear reactions, e.g. at the production target (F0), for example, (p,n) and (^{3}He,n) reactions, are separated through the spectrometer, and focused at F2 where a secondary target is placed for a radioactive beam experiment. The principle of isotope separation is based on the magnetic rigidity analysis and energy losses of particles. A degrader is placed on the intermediate focal point F1. The basic specifications of the magnetic system are listed in Table 2. In the development of flattop-accelerated beam, a primary beam from the RIKEN-AVF cyclotron is path through the CRIB and is focused at F1. The focused beam is disappeared in the following beam course since the magnet D2 is not excited during the beam development.

There are two focusing mode in the development of flattop accelerated beam. The one is a dispersive focusing at focal plane F1. Another is an achromatic focusing mode. The dispersive focusing mode is designed for the CRIB

experiment as mentioned above. This mode focuses the beam horizontally on the focal plane F1. A beam aperture-defining slit before the PPAC is removed to measure the beam profiles. The plastic scintillation counter behind the PPAC covers an effective area of PPAC. The achromatic focusing mode is considered to observe the beam with large cross-section. Although the dispersive focusing mode simulate the CRIB experiment, observation of the beam profiles is difficult because of horizontal position resolution of the PPAC. The achromatic focusing mode resolves this problem. Two focusing modes are alternatively executed in the beam development.
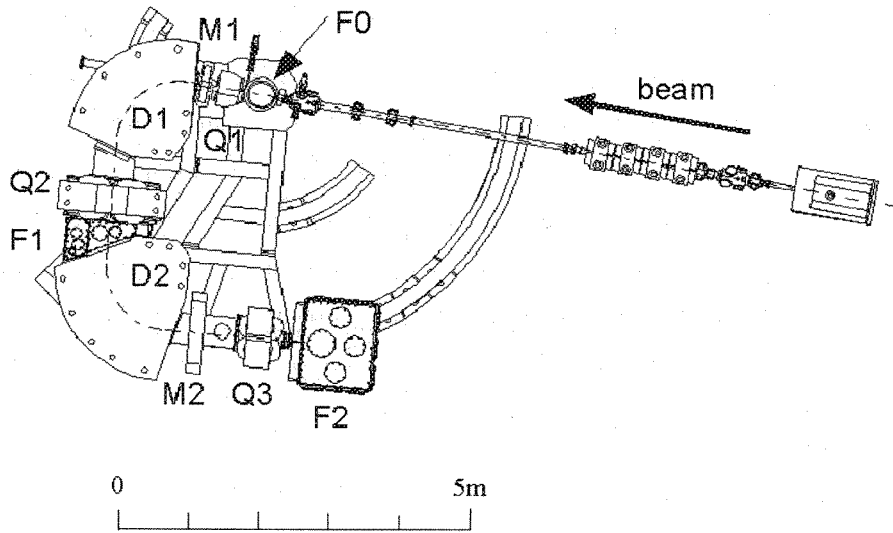

Fig. 10: Top view of the CRIB spectrometer. The F0 is collimator position in the scattering chamber as well as observation position of the beam spot. The position detector PPAC is placed at F1 as a dispersive focal plane [5].

Table 2. Basic magnetic specifications of the CRIB.

Dipole magnet		D1		D2		Unit
Gap height		60		118		mm
Bending angle		95		90		degree
Max magnetic field	Dipole	15		15		KG
	Sextupole	-6.3	0.0	7.4	-2.1	G/cm^2
	Octupole	0	0.0	-130	-20.8	mG/cm^3
Max magnetic rigidity		1.28		1.28		Tm
Weight		18		21		Tons
Quadrupole magnet		Q1	M1	Q2	Q3	M2	Unit
Max magnetic field	Quadrupole	-1.15	-	0.49	-0.75	0.05	KG/cm
	Sextupole	81	-	0.22	0	0	G/cm^2
	Octupole	0	-	-5.5	0	0	mG/cm^3
Weight		0.5	-	3.8	1.1	0.5	Tons

4-3 Optics design of beam transport line

The calculated beam optics from the cyclotron exit to the CRIB-F1 is illustrated in Fig. 11. The primary beam is focused at object point F0 and then guided to F1 in order to tune the experimental instrumentation of the CRIB. The beam optics between the object point F0 and focal plane F1 are designed either achromatic or dispersive focusing mode. Fig.11 shows dispersive focusing mode. Lattice structure of the beam transport line comprises a series of Qf1- Qd1- Qf2- Qd2- Qf3- DMC1- Qd3- Qf4- DMC7- Qd4- Qf5- Qf6- Qd5. The ion beam from the AVF cyclotron is guided to the experimental room, E7, where the CRIB is placed. The vertical bending magnets of DMC1 and DMC7 are placed in the AVF cyclotron room and E7, respectively. Doublet Q magnets (Qd3-Qf4) between both the dipole magnets is rotatable to make a skew Q function. The DMC7 is placed on the rotation angle of 10 degrees in order to guide the beam to the CRIB. The Quartet Q magnets (Qd4-Qf5-Qf6-Qd5) comprise pair of Doublet Q magnets [7]. The mean relative momentum deviation of the beam is 0 % in the calculation. The relative beam momentum spread is 0.1 %. Twiss parameters β_x, α_x, β_z, α_z, D_x, D_z at an injection point of the beam line are 4.561 m, -2.97, 0.985 m, -2.988, 0.859 m, and 0 m, respectively. The right figure in Fig.11 shows calculated beam profile at the CRIB-F1. In this calculation, 500 particles are started at cyclotron exit. The no loss of started particle is confirmed in the right figure when existing wall effect of the transport line is considered. The 90% beam emittances are 7.0 πmmmrad in horizontal and 7.0 πmmmrad in vertical, respectively [10].
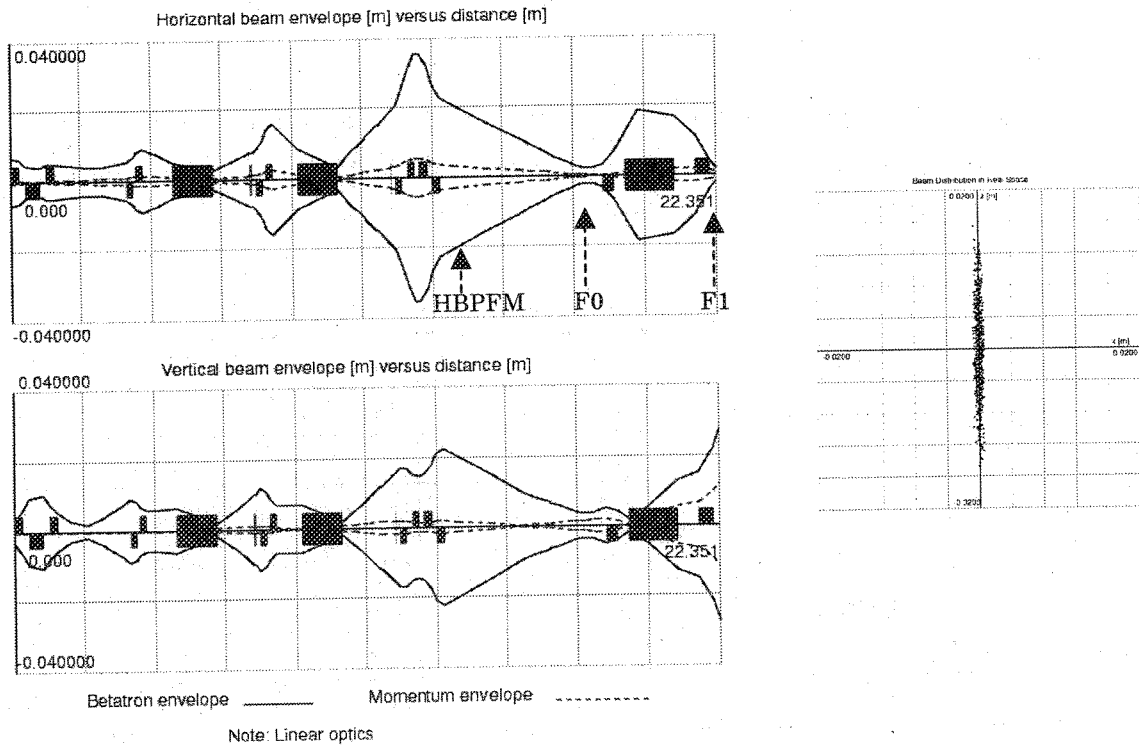

Fig. 11: Calculated beam envelopes of E7 beam line. In the figure, a small block on the center line represents Q magnet. The large block represents dipole magnet. The right figure shows calculated scatter plot of dispersive focused beam at F1. The momentum envelope shows figure at momentum spread of 0.1 %

4-4 Characteristics of the transported beam

There are three kinds of beam diagnostic instruments in the CRIB beam transport line. The first is three wires monitor to show the plot of beam profile in X and Y directions. The second is a Faraday cup to measure the total beam current. The third is a fluorescence screen to show the 3D distribution of the beam. The ion beam is guided to the object point with the aid of beam diagnostic instruments. The beam profile at the CRIB-F0 has been measured by using ZnS screen. The fluorescence screen using Al_2O_3+Cr plate with projection area of 50 x 50 mm^2 was placed at the exit of Quartet Q magnets where the large beam sizes are expected (see Fig.11) [8]. This screen is called HBPFM. A light emitting due to a beam hitting was observed by the TV camera and saved it in the computer memory. Fig. 12-(left) shows a surface plot of the beam profile measured by the HBPFM. The intensity distribution of the measured beam profile is represented by the height of surface plots. A contour map of the measured beam profile is also shown in Fig. 12-(right). There are three islands in the measured beam profiles. It was found in any case that ladder structure, pepper pot structure etc. are formed on the screen. These beam profiles suggest that the beam profile is depending the beam attenuator in the injection line. There are six kinds of beam attenuators in the injection beam line. The attenuation ratios 1/100, 1/10, and 1/2 are combined in series to make a variety of attenuation ratio. The maximum attenuation ratio of designed is 1/20000000. The dependency of the attenuation ratio is considered as an interference pattern formed from two or more ion beams on the screen. Fig.12 shows beam pattern in case of pair of attenuators No.1 (1/100) and No.3 (1/100). Although the MCP in the beam line confirms single turn acceleration, complicated cross-section formed from interference pattern is also appeared whether flattop acceleration system is worked well. It is expected that the same beam profiles would be observed at the downstream such as the focal planes F0 or F1. The observed beam profiles given in Chapter 5 suggest that the fine structure of beam is formed from interference pattern.
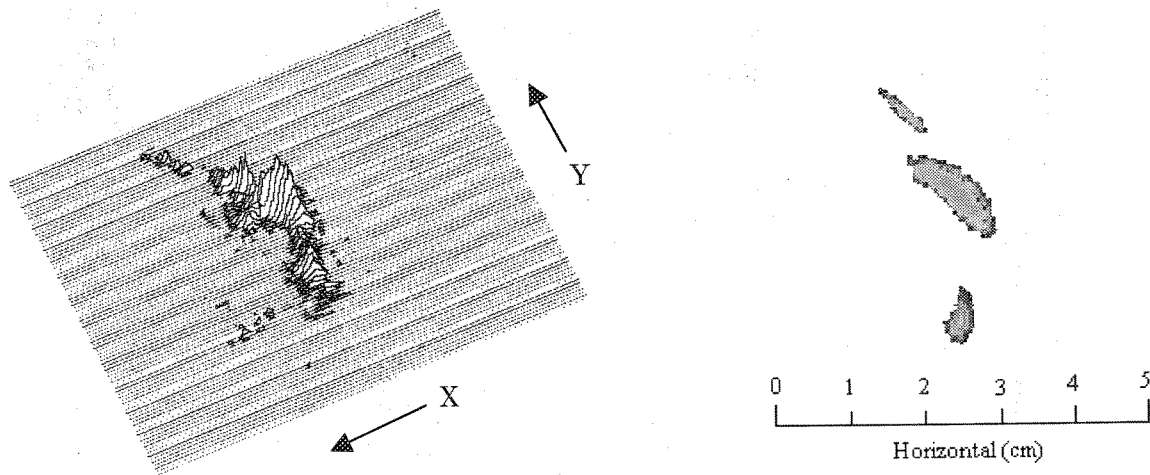

Fig.12: Example of the beam profiles measured by the HBPFM in the CRIB beam line [8]. The left is surface plot and right is contour map, respectively. The contour map comprises three islands formed from interference pattern of the different ion beams.

5. Dispersive focused beam at CRIB F1

5-1 Beam profile measurement

The extracted beam from the AVF cyclotron was transported to the CRIB-F1 as shown in Fig.11. This beam optics is called dispersive focusing mode. Using ZnS coated on a plastic plate carried out the measurement of the beam spot at the object point CRIB-F0. The FWHM of the beam spot was around 2 x 2 mm². After the beam tuning, primary beam current was reduced by acceptable intensity for a parallel plate avalanche counter (PPAC) at the CRIB-F1. Using the PPAC measured the beam profile in detail. Fig. 13 shows summary of beam profiles at the CRIB-F1. The left figure group (4 columns) shows the ordinary accelerated beam (Run #32). The ordinary acceleration is some times called as "FT On". The upper right figure in the left group shows histogram in Y direction. The present figures show the effectively expanded Y direction because of large beta function, β_z, and momentum dispersion function, D_z, at the CRIB-F1. The lower right figure in the left group shows X-Y scatter plots of the beam at the CRIB-F1. Both the figures show that measured beam profiles comprise almost the three peaks. These structural figures are expected from the previous data as shown in Fig. 12. On the other hand, Fig.13 right group shows summary of beam profiles at the flattop acceleration (Run #31). The upper right figure in the right group shows histogram in Y direction. The lower right figure in right group shows X-Y scatter plots of the beam at the CRIB-F1. The lower lefts figure in each group shows RF phase distribution. Whole histograms show that figures of the beam are processed by Gaussian fitting. The 1σ phase spreads of each beam profile are 1.459 ns (= $\Delta\phi_o$) for ordinary acceleration and 1.346 ns (= $\Delta\phi_{ft}$) for flattop acceleration. The phase defining slit was 5.5 mm at ordinary acceleration mode (Run #32) and flattop acceleration mode (Run #31). A saw tooth buncher system was well worked at voltage amplitude of 220 V.

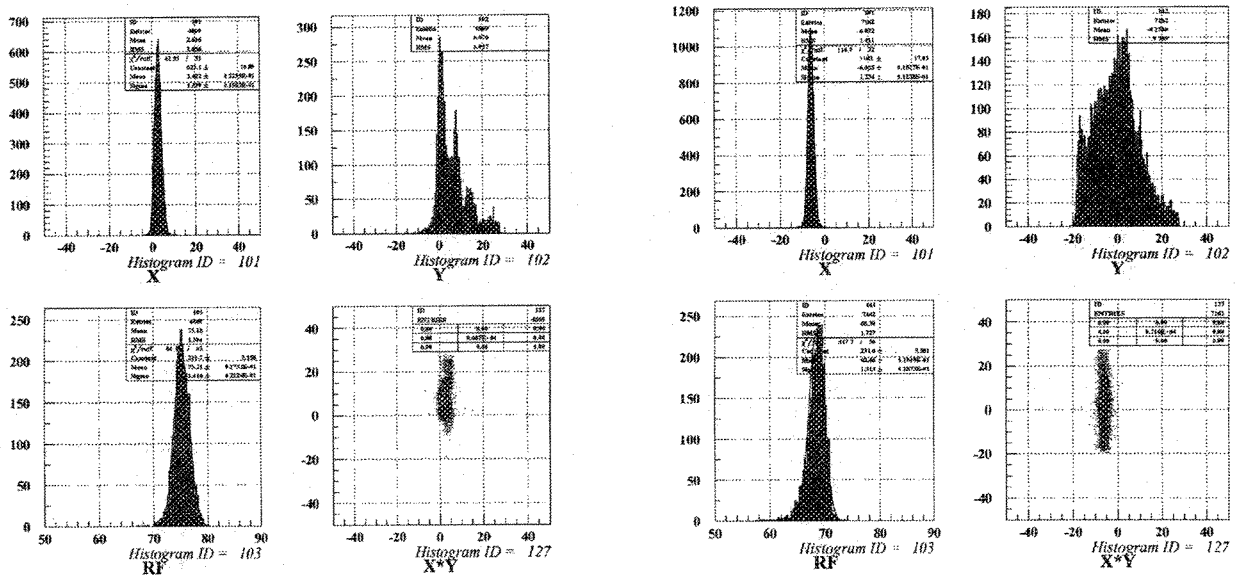Fig. 13: Typical beam profiles measured by the PPAC at the CRIB-F1. The left figure group (4 columns) shows the ordinary accelerated beam (Run #32). The right figure group (4 columns) shows flattop-accelerated beam (Run #31). The figures X and Y in both the group show the histograms in x and y directions. The figure RF in both the group shows time structure. The figure X*Y in both the group shows 2D distributions.

5-2 Energy spread of the dispersive focused beam

The horizontal and vertical profile of the beam focused dispersively on the focal plane F1 was directly measured with the PPAC. The momentum dispersion D_x in horizontal direction is estimated to be 15.8 mm/% from F0 to F1. The energy resolution of the CRIB is mainly limited by the position resolution of the PPAC. Assuming that the position resolution of PPAC is 2 mm FWHM in this measurement, the energy resolving power of the CRIB is estimated to be 395. Beam phase was monitored by a plastic scintillation counter to investigate the time structure of the beam bunch. An rf signal from the Dee voltage picks up is used as a reference signal in the plastic scintillation counter.

In order to choose the counting rate of PPAC below 10^3 cps, using an injection beam attenuator controlled the beam intensity. The observed horizontal width of the beam at F1 for ordinary acceleration was $\sigma = 1.54$ mm which was obtained by a gaussian fitting of the horizontal position distribution. Assuming that the width of the observed spectrum was determined by the natural energy spread of the beam and the energy resolution of the CRIB, and that each distribution had a gaussian shape, the energy spread of the beam itself was estimated to be $\Delta T/T = 0.38$ %. This means that the beam sizes determined by transverse emittances are negligible small at F1.
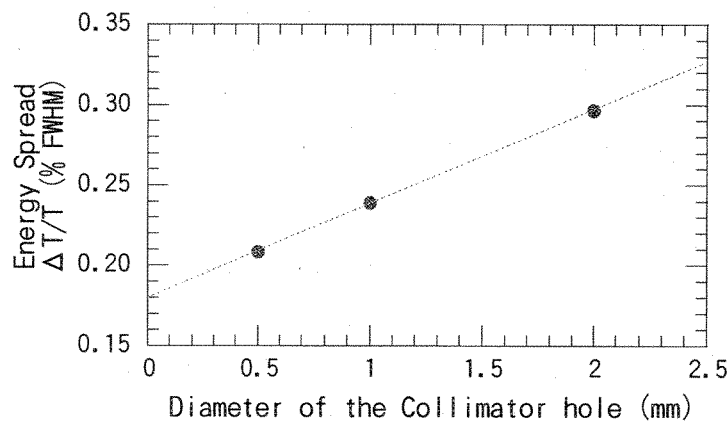

Fig. 14: Dependence of the energy spread on the beam collimation at F0 in the flattop acceleration. The collimation sizes are defined by the hole diameter. The used material for collimator is made of Aluminum plate in 0.5 mm thick.

Thus the flattop- accelerated beam was estimated to be 0.30 % FWHM from the measured value of $\sigma = 1.31$ mm. Slight improvement of the energy spread was observed in the flattop acceleration. Dependence of the energy spread on the beam spot size at F0 for the flattop acceleration is shown in Fig. 14. Two kinds of collimators with a hole of 0.5 mm and 1.0 mm diameter were used for the study. The data for the 2 mm collimation diameter corresponds to the energy spread for a blank collimation. The energy spread decreases proportionally as the collimation size is reduced. The energy spread for the 0.5 mm collimation diameter is estimated to be 0.21 % FWHM.

5-3 particle distributions in the longitudinal phase space

The particle distributions in the longitudinal phase space observed at F1 are shown in Fig. 15. A little dependence

of the momentum on the beam phase was found in the distribution of the ordinarily accelerated particles as shown in the left scatter plot. The distribution shape for the flattop-accelerated particles, shown in the right scatter plot, is almost straight as was expected. The scatter plots in the vertical and horizontal plane, was also measured. The measured scatter plots in this plane show that the vertical scatter is clearly observed since the focal plane F1 is vertical dispersive.
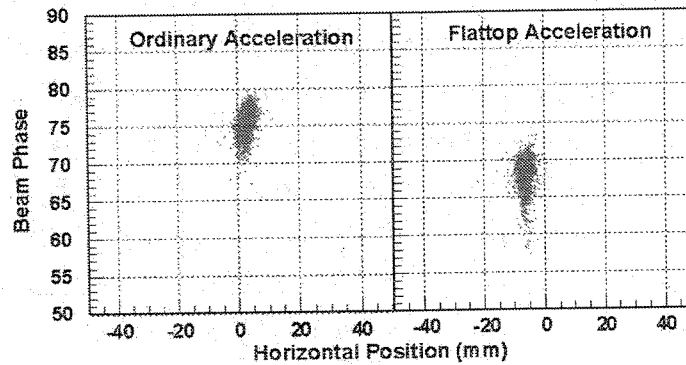

Fig. 15: Correlation between the horizontal position and the beam phase at F1. The left (Run #32) and right (Run #31) scatter plots show particle distributions in the longitudinal phase space for the ordinary acceleration and the flattop acceleration, respectively. The value of beam phase gives arbitrary unit.

6. Achromatic focused beam at CRIB-F1

6-1 Beam profile measurement

The dispersive focused beam at the CRIB-F1 is given in Chapter 5. Although the dispersive focused beam clearly shows the momentum dependence of the beam profile, symmetrical structure in X-Y plane or x-rf plane is not clearly shown. The experiment to measure the transverse beam structure has been done using the experimental set up such as the achromatic setting. The beam optics between the F0 and F1 of the CRIB has been changed to achromatic setting. Calculated beam envelopes are illustrated in Fig. 16. The achromatic setting parameters of Q1, Q2 are −0.7886 kG/cm and −0.1317 kG/cm, respectively. The power feeding cable to the Q2 was modified to exchange the polarity from the focusing to the defocusing. The magnetic rigidity is assumed at 8.54 kGm. After the achromatic setting, the symmetric likes focused beam was observed at the CRIB-F1 as shown in Fig. 16. The particle distributions in the longitudinal phase space observed at F1 with achromatic setting are shown in Fig. 17. This data was taken by the PPAC with high-resolution type (0.76 mm FWHM). A large momentum dependence of the beam phase was found in the distribution of the ordinarily accelerated particles as shown in the left scatter plot.

The distribution shape for the flattop-accelerated particles, shown in the right scatter plot, is almost focused in X*Y plane as was expected. The scatter plots in the vertical and horizontal plane, was also measured. The measured scatter plots in this plane show that the transversal beam scatter is clearly observed since the achromatic setting. The beam width σ_x at flattop acceleration is of 1.34 mm. On the other hand, the measured beam width σ_x at ordinary acceleration is of 4.2 mm. The phase defining slit is chosen at 6.3 mm.
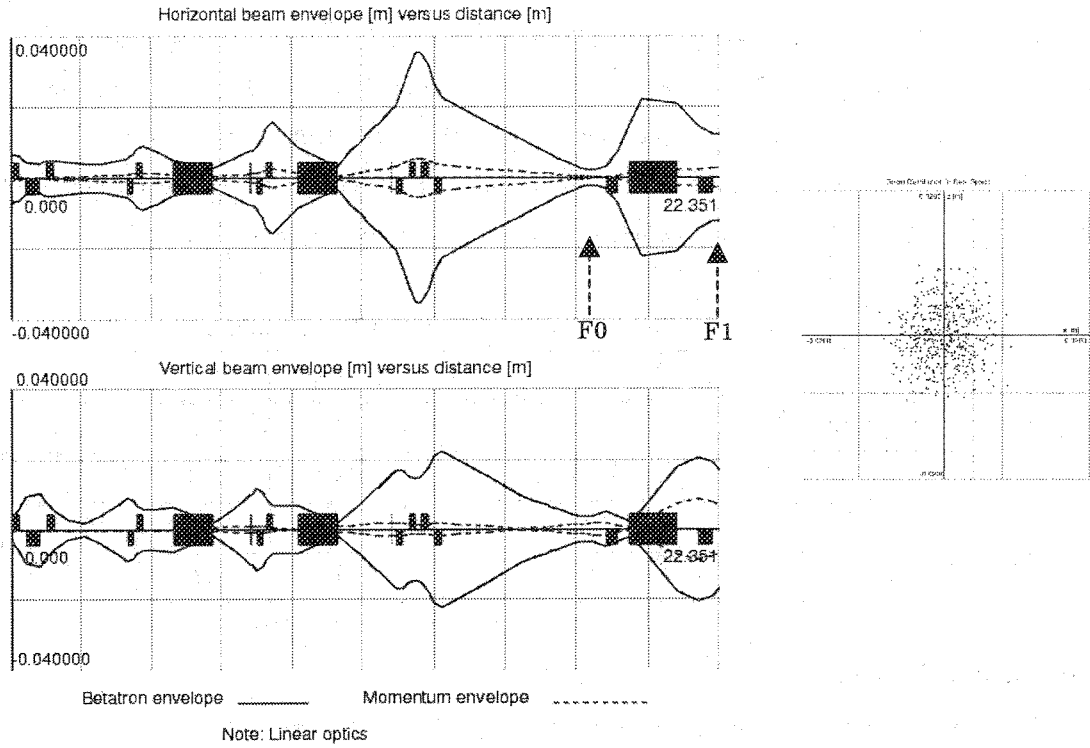
Fig. 16: Calculated beam envelopes of E7 beam line where the achromatic focusing is chosen at F1. In the figure, a symbol is the same to Fig. 11. The right figure is scatter plot at the CRIB-F1. The 500 particles are started at the cyclotron exit and no wall loss is confirmed at the CRIB-F1.

Fig. 17: Typical beam profiles of achromatic focused beam at the CRIB-F1. The left figure group (4 columns) shows the ordinary accelerated beam (Run #13). The right figure group (4 columns) shows flattop-accelerated beam (Run #10). The figures F1_X and F1_Y are particle distribution in X and Y directions, respectively. The figure RF1 shows time structure. The figure X*Y is 2D distribution.

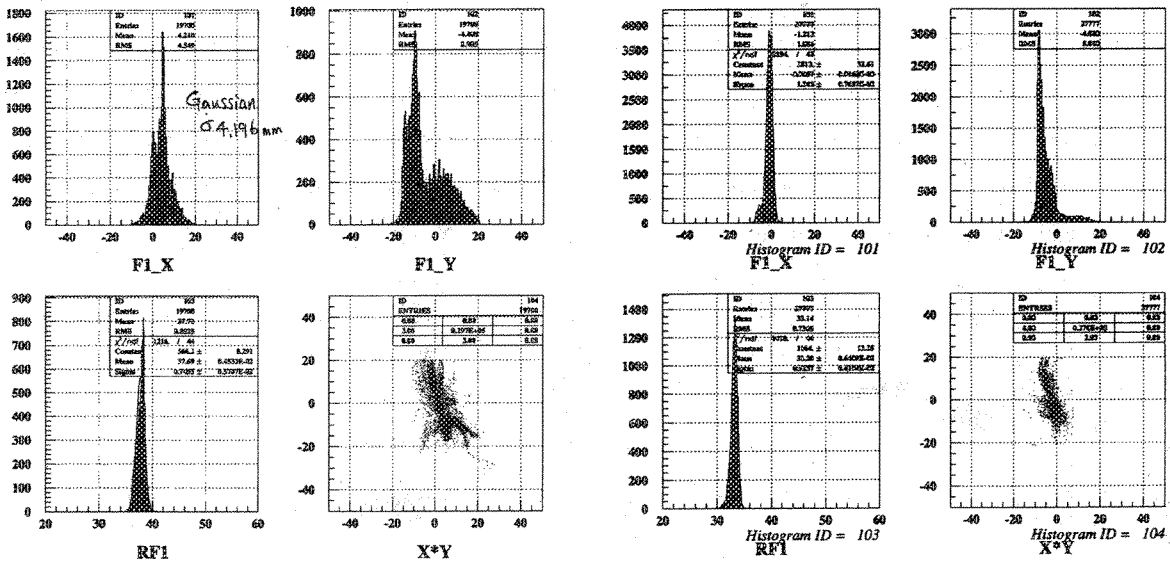Three-wires monitors at Pf1(=C01a), Pf2(=C01b), Pf8(=7A0), and Pf9(=7A1) measured the beam profiles in X-Y directions. Fluorescence screens located at HBPFM and F0 measured the beam profiles. Table 3 compared measured and calculated beam width. The Xm and Ym are measured beam width and the Xc and Yc are calculated beam width. The whole beam width is represented by FWHM. The calculated beam envelopes, Xc and Yc in Table 3 are fitted to 90% beam emittances of $\varepsilon x = \varepsilon y =7$ πmmmrad, respectively. The horizontal beam width measured by pf2 is smaller than calculated one. The reason of difference is under investigation.

Table 3. Measured beam sizes of the CRIB beam line.

Monitor	Pf1	Pf2	Pf8	HBPFM	Pf9	F0
Xm (mm)	3.7	3.5	13.0	17.4	2.8	1.5
Xc (mm)	4.1	6.4	12.8	18.1	2.9	2.2
Ym (mm)	3.0	5.5	9.5	17.0	3.5	1.0
Yc (mm)	3.5	6.0	10.3	18.8	3.0	2.1

6-2 Particle distribution in the longitudinal phase space

Fig.18 shows the examples of the particle distribution in the longitudinal phase space. The ion beam is $^{14}N^{6+}$ 6.4MeV/u. The particle distributions in the longitudinal phase space have been measured for the ordinary acceleration and the flattop acceleration. The left (Run #10) figure represents the ordinary accelerated beam. The right (Run #13) figure shows scatter plots at flattop acceleration. The vertical axis represents the beam phase with scaling unit of 10^{-9} sec. The horizontal scale is physical position of the PPAC at the focal plane F1.

The ordinary accelerated beam shows shape of curved scatter plot. The reason of curved scatter plot is coming from the voltage dependence around the top of sinusoidal waveform like the V1 as shown in Fig. 2. The beam width is determined by the phase defining slit as shown in Fig. 5. The beam phase distribution shows energy spread in the longitudinal phase space. The flattop-accelerated beam shows shapes of condensed scatter plot. Although the scatter plot is including the different energy component, a projection of the horizontal components shows narrowed beam width compared with ordinary acceleration.
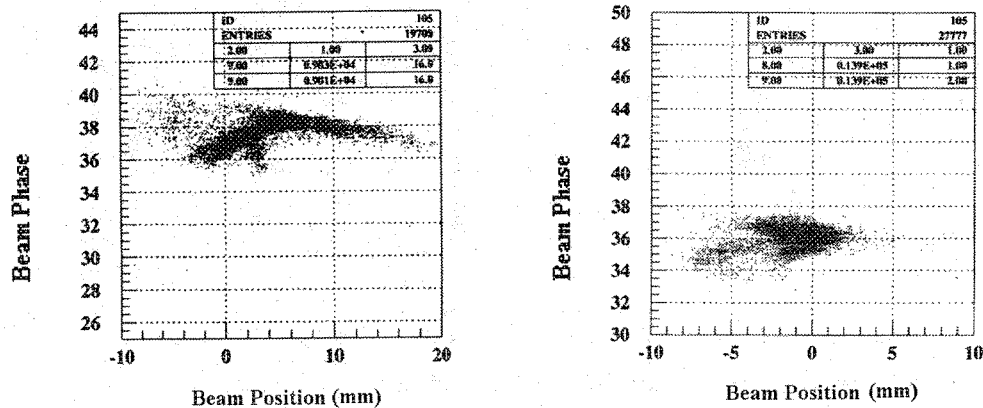

Fig. 18: Correlation between the horizontal position and the beam phase at F1. The left and right figures show the ordinary and the flattop-accelerated beams, respectively.

7. Discussion

7-1 Energy spread

The precise beam width considering the momentum spread $\Delta p/p$, the momentum dispersion D_x, the betatron amplitude β_x and the transversal beam emittance ε_x, has been discussed to evaluate the flattop acceleration.

The momentum spread is given by

$$\frac{\Delta p}{p} = \frac{\sigma_{beam} - \sqrt{\beta_x \varepsilon_x}}{D_x} = \frac{\sqrt{\sigma_{observe}^2 - \sigma_{CRIB}^2} - \sqrt{\beta_x \varepsilon_x}}{D_x}, \qquad (4)$$

where

$$\sigma_{observe} = \sqrt{\sigma_{beam}^2 + \sigma_{CRIB}^2} \quad . \qquad (5)$$

Then the energy spread of FWHM is given by

$$\frac{\Delta T}{T} = 2\sqrt{2\ln 2}\left((1+\gamma^{-1})\frac{\Delta p}{p} \right) . \qquad (6)$$

Actual energy spread measured at dispersive focusing mode is discussed below. Table 4 compared the beam width measured at FT-On and FT-Off. The energy spreads calculated by equation (4) are tabulated in Table 4. The expected beam emittance ε_x is of 7 πmmmrad in Table 4. The calculated energy spread is slightly improved as mentioned in Chapter 5.

Table 4. Energy spreads of 6.4 MeV/u ^{14}N^{6+} beam

Focus type	Dispersive focusing at F1	
Accel. mode	FT On	FT Off
$\sigma_{observe}$	1.31 mm	1.59 mm
σ_{CRIB}	0.851 mm	0. 851mm
σ_{beam}	0.995 mm	1.34 mm
β_x	0.064 m	0.064 m
D_x	1.58 m	1.58 m
$\sqrt{\beta_x \varepsilon_x}$	0.44 mm	0.44 mm
$\Delta p/p$	0.082% FWHM	0.134 % FWHM
$\Delta T/T$	0.162% FWHM	0.268% FWHM

The measured energy spread at achromatic focusing mode shows different result compared with dispersive focusing mode. The detailed measurement result is given in Chapter 6-1. The incident beam was focused at the

CRIB-F1 as shown in Fig. 17. The charge division type PPAC has been used in this experiment. The 1σ position resolution of PPAC is increased by 0.63 mm. The 1σ beam width (σ_{beam}) is 1.34 mm for flattop-accelerated beam. The 1σ beam width (σ_{beam}) is increased by 4.2 mm at ordinary accelerated beam. The momentum dispersion, D_x, at the CRIB-F1 is estimated at 35.3 mm/%. The FWHM momentum spread is given by $\Delta p/p=2.35\sigma_{beam}/D_x$. Thus the $\Delta p/p$ at the flattop acceleration is of 0.089%. The $\Delta p/p$ at the ordinary acceleration is of 0.278 %. We can say that resultant energy spread at the flattop acceleration is reduced by factor 3.

The relationship between the received accelerating energies at the Dees and the measured energy spread of the accelerated beam can be discussed from the point of view of the beam dynamics in the RIKEN-AVF cyclotron. For examples, an accelerating energy gain is depending on the accelerating voltage at the gap along the Dee radii. We are responsible to calculate the accelerating voltage along the Dee radii by using the computer code such as MAFIA. By the way, a low level rf signals has been applied to the main resonator and the flattop resonator respectively in order to simulate the beam dynamics at the actual accelerating voltage. A high impedance voltage probe has been used to measure the rf voltage as function of the Dee radii. The measurement result was compared with the calculation result. It was problem that coincidence good about each other result could not be obtained. Although an inharmonious cause is under investigation, it can expect that electric conditions have changed by insertion of the measurement probe.

7-2 Required accelerating voltage

Instability of the accelerating voltage arose during the study of flattop acceleration. The fundamental voltage dropped frequently due to sparking that occurred in the main resonator. We observed the sparking around the coupling condenser connected to a plate electrode of the final amplifier. We are trying to find the origin and the source of the sparking for the moment. An auto-tuning system to keep the third-harmonic resonance in a flattop resonator didn't work well against the deformation of the resonator caused by temperature change. The measures for flattop resonator temperature stabilization may be needed. The rf accelerating voltage is given by

$$V_{Dee} = \frac{1}{2}\frac{m}{q}(2\pi f_{rev}\rho)^2 (hN_g N_t)^{-1} \quad , \qquad (7)$$

where V_{Dee}, m, q, f_{rev}, ρ, h, N_g, N_t the Dee voltage, mass, charge, revolution frequency, radius of curvature, harmonic number, number of Dee gap, turn number, respectively.

The Dee voltage for 14N6+, 8.8 MeV/u, for example, is calculated by using the given parameters that q/m, f_{rev}, ρ, h, N_g, N_t are 4.1019836×10^7 C/g, 9.14355 MHz, 0.714 m, 2, 2, 105 turns, respectively. The magnetic rigidity, $B\rho$, is expected as 1.0 Tm. The calculated V_{Dee} is 48.832 KV. The terminal voltage V_{cft} at the rf power feeding position of the main resonator is 40.15 KV. The terminal voltage V_{cft} is given by

$$V_{cft} = V_1 \cos\left(L_{Dee} 4 / \lambda\right) - \frac{1}{9}V_1 \cos(3L_{Dee} 4 / \lambda) \quad , \qquad (8)$$

where the L_{Dee} is physical length of 1.54 m. The parameter λ is quarter wavelength of the main resonator. The parameter λ is given by the kc/Frf where the k, c, and Frf are shorting constant, light velocity, and resonant frequency.

The shorting constant k is around 0.6 at resonant frequency of 12 MHz. The constant k is given by the relationship between the shorting length and resonant frequency of the main resonator [9]. The second term in the equation (8) gives terminal voltage generated by the flattop cavity. The voltage except second term in the equation (8) gives V_{cl}. The designed Dee voltages required for the CRIB experiments are listed in Table 5. Table 5 also compared the rf voltage, V_{cft}, at a ceramic ring as a supporting insulator of the main resonator. The electric discharge around the ceramic ring is briefly discussed in Chapter 3. The breakdown voltage of the ceramic ring is 35 kV. The breakdown voltage limited the electric discharge voltage, V_c, of 35 kV. The calculated V_{cft} in Table 5 almost exceed the V_{cl} and some kinds of V_{cft} overcome the breakdown voltage 35 KV of the ceramic ring. The electric discharge is actually found near the rf power amplifier 4CW50000E. Operating Dee voltage keeps 35 kV or less in the present operation. The rf power condenser for the plate circuit of the 4CW50000E is high voltage type. In order to prohibit the negative power loading at the screen grid of the 4CW50000E, an impedance matching technique is to be employed against change of resonance frequency of the main resonator. It is recommended that a tunable vacuum condenser is to be adopted between the plate circuit of the 4CW50000E and the inner conductor of the main resonator.

Table 5. The rf accelerating voltages required for the CRIB experiments

Beam	T (MeV/u)	Br (Tm)	Frf (MHz)	V_{Dee} (KV)	V_1 (KV)	V_{3rd} (KV)	V_{cl} (KV)	V_{cft} (KV)
14N5+	7.0	1.07	16.3	46.63	52.09	5.78	36.67	40.80
14N5+	8.8	1.20	18.3	51.0	57.38	6.38	36.32	41.95
14N5+	10.0	1.28	19.5	58.6	65.93	7.32	38.70	45.67
14N6+	6.4	0.854	15.6	35.5	40.0	4.40	29.12	31.95
14N6+	8.8	1.0	18.3	48.8	54.91	6.10	34.76	40.15
14N6+	10	1.07	19.5	55.5	62.46	6.94	36.67	43.28
14N6+	12.8	1.20	21.9	62.0	69.76	7.75	34.11	41.86
14N7+	10.0	0.92	19.5	41.9	47.14	5.23	27.67	32.66
12C5+	7.0	0.91754	16.3	39.9	44.90	4.98	31.61	35.17

7-3 Turn separation

Most of the losses in isochronous cyclotron usually occur at the deflector septum during extraction. The radius gain between turns should be increases as much as possible to decrease these losses. The radius gain per turn due to the energy gain, in absence of any other off-centering mechanism is given approximately;

$$\Delta R = R \frac{\Delta E}{E} \frac{\gamma}{\gamma + 1} \frac{1}{v_r^2} \qquad (9)$$

where the ΔR, R, ΔE, E, γ, v_r, are the turn separation, the extraction radius, the energy gain per turn, the extraction energy, the relativistic factor ($= 1/\sqrt{1-\beta^2}$) and the radial focusing frequency.

Increasing the voltage of the rf system is the obvious way of increasing the energy gain, but it is limited by electric discharge and power limitations. The energy gain ΔE is depending on Dee voltage and v_r is nearly 1. In the present study, an expected turn numbers at ordinary acceleration is of 105. The resultants turn number at the flattop acceleration increases by 11 %, since it is inversely proportional to the peak voltage V_{Dee} of 32.4 KV at 6.4 MeV/u $^{14}N^{6+}$ beam. (Be compared with Table 5) The increase of turn number in the flattop acceleration suggests that energy-spread ΔT is decreased compared with ordinary acceleration. The energy spread of each accelerated beam is equivalent to the 1σ phase spreads such as 1.539 ns ($=\Delta\phi_o$) for ordinary acceleration (Run #32) and 1.346 ns ($= \Delta\phi_{ft}$) for flattop acceleration (Run #32). The ratio of phase spreads of (($\Delta\phi_{ft} - \Delta\phi_o$)/ $\Delta\phi_o$) x 100% = -12.5 % is roughly equivalent to the increase of the turn number of 11 %. Note that the phase defining slit in the injection section is set at 5.5 mm. The beam property in the cyclotron is changed due to increase of turn number of the beam. It is in turn that Twiss parameter at exit of cyclotron is changed. The measured result shows that focal point of the F0 is shifted to down stream where the inside of the bending magnet D1.

7-4 Beam transmission

We have studied the beam transmission, that is the ratio of the beam intensity at the extraction part of the AVF cyclotron (i3) to that at the injection point (i1). An ion source is HyperECR developed by CNS, Univ. of Tokyo. The extracted beam was focused by Doublet Q magnets and analyzed by the 90 degrees C-type bending magnet. After the mass analysis, the analyzed beam is focused by a solenoid magnet and bent down by the 90 degrees window-frame type 90 degrees magnet. The transmission efficiency, for example, is 29 % at $^{14}N^{6+}$ ion beam with acceleration energy of 6.4 MeV/u. Beam transmission efficiencies with the flattop acceleration for the $^{14}N^{6+}$ ion beam from the HyperECR were measured. The results are shown in Table 6. In these measurements, an rf buncher is placed just above the upper magnetic yoke of the cyclotron to give a flight path length of about 2 m. A saw tooth amplitude of the rf buncher was chosen at 220~225 V. In order to control the counting rate of the PPAC at the CRIB-F1, repetition rate of the rf buncher was controlled together with the beam attenuator. The transmission efficiency in the beam transport line has been measured by using the Faraday cup monitor. The measured transmission efficiency is almost 100 % under the flattop acceleration. The first and thermal neutron monitors are located along the beam line in X-Y directions. After the beam optics tuning, the neutron monitors detect no neutron flux.

Table 6. Beam transmission efficiencies with the flattop acceleration for the $^{14}N^{6+}$ ion beam.

Measuring device	FT Off (%)	FT On (%)
Probe at radius of 7.5 cm on median plane	31.3	36.0
Probe at radius of 64.5 cm on median plane	26.3	29.8
FC-3 on extraction line	21.0	29.6

8. Conclusion

The flattop acceleration system was installed in the RIKEN-AVF cyclotron. The flattop-accelerated beam has been developed for the low-energy radioisotope beam separator CRIB. The transmission efficiency of the injected beam is slightly increased by using the flattop acceleration system. The energy spread of the flattop-accelerated beam has been improved by 1/3 compared with the ordinary acceleration. The flattop accelerating voltage for the CRIB experiments has been discussed. The electrical insulation performance of the substrates and other electronical parts in the rf accelerating cavities is now being developed.

Acknowledgments

References

[1] Y. Yano, Proc. 12th Int. Conf. On Cyclotrons and their Applications, Berlin, eds. B. Matin and Z. Ziegler (World Scientific, 1989) p.13.

[2] J. L. Conradie et al.: Proc. 14th Int. Conf. on Cyclotrons and Their Applications, Cape Town, South Africa, p. 249 (1995).

[3] T. Katayama et al.: CNS Ann. Rep. 2000. p.7 (2000).

[4] S. Kohara et al.; RIKEN Accel. Prog. Rep. 35, p.272 (2001).

[5] T. Teranishi et al. CNS-REP-39, Oct. 2001.

[6] A. Goto, et. al., Proc. of the 12th Int. Conf. on Cyclotrons and Their Applications, pp439-442 (1989).

[7] S.Watanabe et al. CNS Ann. Rep. 2000. p.9 (2000).

[8] S.Watanabe et al. CNS Ann. Rep. 2000. p.60 (2000).

[9] S.Kohara et al. Proc. of Cyclotron and their Applications 98, Caen, 14-19 June 1998, pp219-222. See Table 1.

[10] N.Inabe et al. RIKEN Accel. Prog. Rep.28, p.158 (1995).

Appendix 1; MAD 8 file for beam transport line

TITLE "crib0907"

QC011: QUADRUPOLE, L= 2.5000000000E-01, K1= 7.1971196216E+00
DRF2: DRIFT, L= 2.0000000000E-01
QC012: QUADRUPOLE, L= 4.5000000000E-01, K1=-6.1241490291E+00
DRF3: DRIFT, L= 2.0000000000E-01
QC013: QUADRUPOLE, L= 2.5000000000E-01, K1= 4.9200000000E+00
DRF4: DRIFT, L= 5.0000000000E-01
pf1: DRIFT, L= 3.5000000000E-02
drf41: DRIFT, L= 4.5000000000E-01
stc01: SBEND, L= 1.0000000000E-02, ANGLE= 0.0000000000E+00, &
  K1=-1.0000000000E-02, E1= 0.0000000000E+00, E2= 0.0000000000E+00, &
  K2= 0.0000000000E+00, HGAP= 0.0000000000E+00, FINT= 0.0000000000E+00
DRF5: DRIFT, L= 5.5000000000E-01
LR: DRIFT, L= 3.5000000000E-02
drf50: DRIFT, L= 5.0500000000E-01
fc1: DRIFT, L= 3.5000000000E-02
DRF51: DRIFT, L= 2.4500000000E-01
QC021: QUADRUPOLE, L= 2.0000000000E-01, K1=-1.0091301066E+01
DRF52: DRIFT, L= 1.1000000000E-01
QC022: QUADRUPOLE, L= 2.0000000000E-01, K1= 1.0091301066E+01
DRF53: DRIFT, L= 3.4000000000E-01
pf2: DRIFT, L= 3.5000000000E-02
DRF54: DRIFT, L= 5.7500000000E-01
DMC1: SBEND, L= 1.2566400000E+00, ANGLE= 1.5707960000E+00, &
  K1= 0.0000000000E+00, E1= 0.0000000000E+00, E2= 0.0000000000E+00, TILT, &
  K2= 0.0000000000E+00, HGAP= 3.0000000000E-02, FINT= 0.0000000000E+00
DRF6: DRIFT, L= 6.9000000000E-01
DRF7: DRIFT, L= 3.0500000000E-01
stc10u: SBEND, L= 1.0000000000E-02, ANGLE= 0.0000000000E+00, &
  K1= 0.0000000000E+00, E1= 0.0000000000E+00, E2= 0.0000000000E+00, &
  K2= 0.0000000000E+00, HGAP= 0.0000000000E+00, FINT= 0.0000000000E+00
drf70: DRIFT, L= 6.5000000000E-02
DRF71: DRIFT, L= 1.3500000000E-01
stc10d: SBEND, L= 1.0000000000E-02, ANGLE= 0.0000000000E+00, &
  K1= 0.0000000000E+00, E1= 0.0000000000E+00, E2= 0.0000000000E+00, &
  K2= 0.0000000000E+00, HGAP= 0.0000000000E+00, FINT= 0.0000000000E+00
drf712: DRIFT, L= 5.5000000000E-02
drf713: DRIFT, L= 1.2250000000E-01
QC111: QUADRUPOLE, L= 2.0500000000E-01, K1=-1.1006217940E+01
DRF8: DRIFT, L= 1.0500000000E-01
QC112: QUADRUPOLE, L= 2.0500000000E-01, K1= 1.0999143043E+01
DRF9: DRIFT, L= 7.9250000000E-01
DMC7: SBEND, L= 1.2566400000E+00, ANGLE=-1.5707960000E+00, &
  K1= 0.0000000000E+00, E1= 0.0000000000E+00, E2= 0.0000000000E+00, TILT, &
  K2= 0.0000000000E+00, HGAP= 3.0000000000E-02, FINT= 0.0000000000E+00
DRF10: DRIFT, L= 4.5500000000E-01
drf100: DRIFT, L= 2.3500000000E-01
DRF101: DRIFT, L= 2.0000000000E-01
st7a0: SBEND, L= 1.0000000000E-02, ANGLE= 0.0000000000E+00, &
  K1= 0.0000000000E+00, E1= 0.0000000000E+00, E2= 0.0000000000E+00, &
  K2= 0.0000000000E+00, HGAP= 0.0000000000E+00, FINT= 0.0000000000E+00
drf102: DRIFT, L= 3.6500000000E-01

pf8: DRIFT, L= 1.0000000000E-02
drf104: DRIFT, L= 4.0500000000E-01
st7a1: SBEND, L= 1.0000000000E-02, ANGLE= 0.0000000000E+00, &
  K1=-1.0000000000E-03, E1= 0.0000000000E+00, E2= 0.0000000000E+00, &
  K2= 0.0000000000E+00, HGAP= 0.0000000000E+00, FINT= 0.0000000000E+00
drf105: DRIFT, L= 1.5000000000E-01
Q7N11: QUADRUPOLE, L= 2.3000000000E-01, K1=-4.7720365235E+00
DRF11: DRIFT, L= 1.7000000000E-01
Q7N12_1: QUADRUPOLE, L= 2.3000000000E-01, K1= 4.1634755198E+00
DRF12: DRIFT, L= 1.7000000000E-01
Q7N12_2: QUADRUPOLE, L= 2.3000000000E-01, K1= 4.1634755198E+00
DRF13: DRIFT, L= 1.7000000000E-01
Q7N13: QUADRUPOLE, L= 2.3000000000E-01, K1=-4.7720365235E+00
DRF14_1: DRIFT, L= 4.5500000000E-01
HBPFM: DRIFT, L= 1.0000000000E-03
DRF14: DRIFT, L= 1.0290000000E+00
DRF15: DRIFT, L= 1.0000000000E+00
drf150: DRIFT, L= 3.7000000000E-01
st7a2: SBEND, L= 1.0000000000E-02, ANGLE= 0.0000000000E+00, &
  K1= 0.0000000000E+00, E1= 0.0000000000E+00, E2= 0.0000000000E+00, &
  K2= 0.0000000000E+00, HGAP= 0.0000000000E+00, FINT= 0.0000000000E+00
drf151: DRIFT, L= 4.8000000000E-01
st7a3: SBEND, L= 1.0000000000E-02, ANGLE= 0.0000000000E+00, &
  K1= 0.0000000000E+00, E1= 0.0000000000E+00, E2= 0.0000000000E+00, &
  K2= 0.0000000000E+00, HGAP= 0.0000000000E+00, FINT= 0.0000000000E+00
DRF16: DRIFT, L= 0.0000000000E+00
drf160: DRIFT, L= 2.4000000000E-01
gv160: DRIFT, L= 1.0000000000E-02
DRF17: DRIFT, L= 5.0000000000E-01
pf9: DRIFT, L= 1.0000000000E-02
drf170: DRIFT, L= 2.0000000000E-01
drf171: DRIFT, L= 2.0000000000E-01
drf172: DRIFT, L= 2.0000000000E-01
drf173: DRIFT, L= 1.5000000000E-02
target: SOLENOID, L= 1.0000000000E-02, KS= 0.0000000000E+00
CRIBdrift0: DRIFT, L= 9.5000000000E-02
CRIBdrift201: DRIFT, L= 2.8150000000E-01
CRIBQ1: QUADRUPOLE, L= 3.7700000000E-01, K1=-6.6998440000E+00
CRIBdrift301: DRIFT, L= 3.6650000000E-01
CRIBBEND1: SBEND, L= 3.9270000000E-01, ANGLE= 4.3633200000E-01, &
  K1= 0.0000000000E+00, E1= 2.3654000000E-01, E2= 0.0000000000E+00, &
  K2= 0.0000000000E+00, HGAP= 0.0000000000E+00, FINT= 0.0000000000E+00
CRIBBEND2: SBEND, L= 1.0996000000E+00, ANGLE= 1.2217300000E+00, &
  K1= 0.0000000000E+00, E1= 0.0000000000E+00, E2= 3.4907000000E-01, &
  K2= 0.0000000000E+00, HGAP= 0.0000000000E+00, FINT= 0.0000000000E+00
CRIBdrift302: DRIFT, L= 6.6200000000E-01
CRIBQ2: QUADRUPOLE, L= 4.7600000000E-01, K1= 2.8541720000E+00
CRIBdrift303: DRIFT, L= 2.0200000000E-01

crib0907: LINE=(QC011,DRF2,QC012,DRF3, &
                QC013,DRF4,pf1,drf41, &
                stc01,DRF5,LR,drf50, &
                fc1,DRF51,QC021,DRF52, &
                QC022,DRF53,pf2,DRF54, &
                DMC1,DRF6,DRF7,stc10u, &
                drf70,DRF71,stc10d,drf712, &

```
drf713,QC111,DRF8,QC112, &
DRF9,DMC7,DRF10,drf100, &
DRF101,st7a0,drf102,pf8, &
drf104,st7a1,drf105,Q7N11, &
DRF11,Q7N12_1,DRF12,Q7N12_2, &
DRF13,Q7N13,DRF14_1,HBPFM, &
DRF14,DRF15,drf150,st7a2, &
drf151,st7a3,DRF16,drf160, &
gv160,DRF17,pf9,drf170, &
drf171,drf172,drf173,target, &
CRIBdrift0,CRIBdrift201,CRIBQ1,CRIBdrift301, &
CRIBBEND1,CRIBBEND2,CRIBdrift302,CRIBQ2, &
CRIBdrift303)
```

Use, crib0907
Print, full
Twiss, save
Return